Regular & Chaotic Dynamics
September 2021, Volume 26 Issue 5 Pages 543-561
https://doi.org/10.1134/S1560354721050063
https://archimer.ifremer.fr/doc/00730/84222/

Interaction of an Upwelling Front with External Vortices: Impact on Cross-shore Particle Exchange

de Marez Charly [1, *], Carton Xavier [1, *]

[1] Univ Brest, Lab Oceanog Phys & Spatiale LOPS, IUEM, Rue Dumt Durville, F-29280 Plouzane, France.

Corresponding authors :Charly de Marez, email address : charly.demarez@univ-brest.fr ; Xavier Carton, email address : xcarton@univ-brest.fr

Abstract :

Coastal upwellings, due to offshore Ekman transport, are more energetic at the western boundaries of the oceans, where they are intensified by incoming Rossby waves, than at the eastern boundaries. Western boundary upwellings are often accompanied by a local vortex field. The instability of a developed upwelling front and its interaction with an external vortex field is studied here with a three-dimensional numerical model of the hydrostatic rotating Navier-Stokes equations (the primitive equations). The baroclinic instability of the front leads to the growth of meanders with 100-200 km wavelength, in the absence of external vortex. On the f-plane, these waves can break into a row of vortices when the instability is intense. The beta-effect is stabilizing and strongly decreases the amplitude of meanders. Simulations are then performed with a front initially accompanied by one or several external vortices. The evolutions in this case are compared with those of the unstable jet alone. On the f-plane, when an external vortex is close to the front, this latter sheds a long filament which wraps up around the vortex. This occurs over a period similar to that of the instability of the isolated front. Cyclones are more efficient in tearing such filaments offshore than anticyclones. On the beta-plane, the filaments are short and turbulence is confined to the vicinity of the front. At long times, waves propagate along the front, thus extending turbulence alongshore. The initial presence of a vortex alley leads to a stronger destabilization of the front and to a larger cross-shore flux than for a single vortex, with many filaments and small vortices pushed far offshore. In the ocean, this cross-shore exchange has important consequences on the local biological activity.

Keywords : coastal upwelling front, vortices, filaments, baroclinic instability, frontal waves, particle motion and tracking

1. Introduction

The Arabian Sea, in the North-Western Indian Ocean, is the seat of oceanographic processes which interact dynamically (see Fig. 1). These physical processes in turn, influence the regional biological activity of the ocean. This sea evolves under the influence of monsoon winds (north-easterlies in winter and south-westerlies in summer; Schott & Fischer, 2000) and of a strong evaporation rate (Privett, 1959). The strong winds induce a cyclonic regional circulation in winter and an anticyclonic regional one in summer. Moreover, these winds generate Rossby waves near the western coast of India (Brandt et al., 2002). These waves propagate westward and they can strengthen large, long-lived eddies, like the Great Whirl near the coast of Somalia (Vic et al., 2015) and the Ras al Hadd dipolar eddy South of Oman (Ayouche et al., 2021) (eddies are oceanic vortices). The Arabian Sea is populated with many eddies (Bruce et al., 1994; Al Saafani et al., 2007; Trott et al., 2019). Such eddies are formed in particular by the instability of coastal currents and of the regional gyre currents.

A second main feature of the Arabian Sea are two western boundary upwellings (near Somalia and South of Oman), as the wind blows parallel to the coast and northwestward in summer (Sastry & d'Souza, 1972; Bruce, 1974; Elliott & Savidge, 1990; Currie, 1992; Shi et al., 2000; Fischer et al., 2002; Piontkovski & Al-Jufaili, 2013; Vic et al., 2017). In upwellings, the Ekman drift due to the wind pushes the surface water offshore leading to an outcropping of deeper and colder water from depths of 150 m. This cold water (which can be 5°C cooler than the Arabian Sea surface water) is rich with nutrients, favoring the local biological activity. And indeed, this upwelling region is an intense fishing area. When the upwelling is developed (in August/September), the sea surface height near the coast can lie 30 cm below the offshore sea surface and a northeastward current, the Oman Coastal Current, flows offshore. Western boundary upwellings are more energetic than their eastern boundary counterparts because they absorb energy from incoming Rossby waves. The temperature and salinity fronts which bound the upwelling region offshore are not steady. They often meander and they may form cold filaments. Capes play an important role in the offshore growth and protrusion of cold filaments from upwellings (Currie, 1992; Shi et al., 2000; Meunier et al., 2010). These filaments can extend offshore over more than 250 km and bring nutrients into the oligotrophic surface ocean (Manghnani et al., 1998). South of Oman, the upwelling lasts for the whole summer and interacts with the local eddy field (see Fig. 5 of Shi et al., 2000). The upwelling front and current can form meanders and eddies, either by instability or *via* the interaction with the eddies (see Fig. 5 of Sastry & d'Souza, 1972). The evolution of an upwelling front and coastal current in the presence of external vortices, and its comparison with the evolution of an unstable front in the absence of such vortices, is the subject of the present paper, with application to the Arabian Sea (again, see Fig. 1).

The structure and stability of upwelling systems, with fronts and currents, have been the subject of many previous studies (Yoshida, 1955; Hidaka, 1972; Pedlosky, 1974; McCreary, 1981; Csanady, 1982, to name a few). The first studies aimed at understanding the spin-up of the upwelling as the wind starts to blow and before it becomes a well established front associated with a geostrophic current. In particular, the role of the frictional boundary layers in the formation of the upwelling was investigated (Pedlosky, 1974). The importance of the topographic constraint on the deep boundary layer was analyzed (Pedlosky, 1978a,b). Analytical solutions of the density and velocity structure were provided for a time varying wind stress forcing the upwelling. In particular, the formation of a sub-surface counter-current was studied with regard to the vertical mixing of heat and momentum (McCreary, 1981). For an upwelling south of a zonal coast, an eastward baroclinic current builds up as the offshore front steepens. When the wind stress has a longshore variation, Kelvin waves propagate along the coast, away from the upwelling region. The alongshore flow deviates from geostrophy. Ageostrophic velocities perpendicular to the coast then form a two-cell vertical circulation (Suginohara, 1977).

In our study, we investigate the instability of the geostrophic current associated with the offshore upwelling front, or how it interacts with an external eddy field; we assess the consequences of these interactions on cross-shore transport. The interaction between a zonal current and a single external eddy has been the subject of several studies. Pratt & Stern (1986) studied the growth and detachment of an eddy from a potential vorticity front in a one-layer model. Stern & Flierl (1987) considered the interaction between a single eddy and a zonal potential vorticity front in a one-layer model (with finite or infinite radius of deformation). They showed that, in the linear stage of the interaction, the surface integral of vorticity in the meander of the front is equal and opposite to the area integral of the eddy vorticity. This leads to a dipolar effect which can advect the eddy along the front. Vandermeirsch et al. (2003a,b) determined the conditions under which an eddy can cross a potential vorticity front meridionally, in one and two-layer models. The existence of a stagnation point (a hyperbolic point in the flow field) was found as a necessary condition for this crossing. This condition is identical for the detachment of an eddy from an unstable front (Capet & Carton, 2004). These latter authors found that the circulation of the detached eddy was proportional to that enclosed within a wavelength of the meandering front, extending offshore to the stagnation point.

This paper is organized as follows. Section 2 describes the numerical model and the analysis tools. In particular, the novelty of this paper lies in the use of a three-dimensional model (see supplementary information for the presentation of the 3D evolution of some simulations discussed in this study). Section 3 details the numerical results of the upwelling current instability, in the absence of vortices. The results are analyzed with respect to the characteristic wavelengths of the meanders growing on the current and of the inshore and offshore transports. Section 4 considers the nonlinear evolution of the front in the presence of a single vortex offshore. Cyclone-anticyclone asymmetry is considered since the flow is not quasi-geostrophic. Section 5 considers the situation where multiple vortices exist South of the front, as observed in the Arabian Sea. Section 6 characterizes the cross-shore exchanges with particle tracking. Conclusions follow.

2. Methods

2.1. The numerical simulations

In this section, we present the idealized model runs performed for this study. The aim of these runs is to study the instability of an upwelling front and to simulate the interaction of an upwelling front with one or several vortices.

2.1.1. Numerical setup and domain

The simulations are carried out in a 3D hydrostatic primitive equation framework. They are performed using the Coastal and Regional Ocean COmmunity (CROCO) model (Shchepetkin & McWilliams, 2005). This model solves the hydrostatic primitive equations for the velocity, temperature, and salinity, using a full equation of state for seawater (Shchepetkin & McWilliams, 2011). The simulations performed integrate the primitive equations for 1 year. The numerical settings are similar to previous simulations performed in an idealized context (see *e.g.* Ménesguen et al., 2018; de Marez et al., 2020b): horizontal advection terms for tracers and momentum are discretized with fifth-order upwind advection schemes (UP5); the explicit horizontal viscosity and diffusivity are set to zero, since the UP5 scheme damps dispersive errors; the vertical advection is discretized with a fourth-order centered parabolic spline reconstruction (Splines scheme). Further discussion about these parameterizations can be found in Klein et al. (2008) or Ménesguen et al. (2018). Vertical mixing of tracers and momentum is done using a K-profile parametrization (KPP, Large et al., 1994), and there is no bottom friction. Simulations have 32 terrain-following vertical levels, which are stretched such that the vertical resolution is $\Delta z \sim 8$ m at the surface, and $\Delta z \sim 120$ m at the bottom. The horizontal resolution is 5 km. The domain is square, with a length $L_{\text{domain}} = 2000$ km or $L_{\text{domain}} = 3000$ km in vortex alley simulations (see details below). The bottom is flat and 2000 m deep. We set the Coriolis parameter to $f = f_0 = 10^{-4}\,s^{-1}$ or $f = f_0 + \beta y$, with $\beta = 2 \times 10^{-11}\,\mathrm{m}^{-1}\,\mathrm{s}^{-1}$ and y the meridional coordinate. The northern and southern boundaries are closed, with a 10 km wide sponge layer to avoid the generation of spurious boundary dynamics. A zonal periodic condition is chosen at the eastern and western boundaries such that the domain is a zonal channel.

We initialize an analytical background stratification $N(z)$, which fits the average ambient stratification in the five major oceanic basins, similarly as in de Marez et al. (2020a,c):

$$N(z) = N_0 + N_1\, e^{z/z_h}, \tag{1}$$

with $z < 0$ the vertical coordinate, $N_1 = 9 \times 10^{-3}\,\mathrm{s}^{-1}$, $z_h = 150\,\mathrm{m}$, and $N_0 = 7 \times 10^{-3}\,\mathrm{s}^{-1}$. Integrating this stratification from the surface (where $\rho(z = 0) = 1030\,\mathrm{kg\,m}^{-3}$), gives the ambient density background $\rho(z)$; the temperature background $T(z)$ is obtained by inverting the TEOS-10 equation of state for seawater McDougall & Barker (2011) and assuming a constant salinity background $S(z) = 35\,\mathrm{psu}$. The model is initialized with these temperature and salinity background profiles.

2.1.2. Components of simulations

Upwelling front. We chose to study the evolution of the upwelling front once it is established by the wind forcing. This established front is the initial condition of our simulations, which are then run in free decay. These simulations determine the further, unforced, evolution of this front. Not adding surface forcing in the simulations allows us to analyze specifically the front instability or the front-vortex interaction as a classical initial-value problem. Our simulations have an application to the ocean when the time scales of the evolution are shorter than those of the forcing. For other cases, simulations with forcing, or with a relaxation towards a prescribed state, will be performed in a follow-up of this study. It must be noted that free-decay simulations have often been used in studies of oceanic flow stability, since they produce instability waves which depend only on the current and not on the forcing.

We simulate the presence of an upwelling front by initializing a zonal jet of a given velocity profile, similarly as in Barth (1994); this velocity profile has the form:

$$u_{up} = V_0^{up}\, \mathrm{e}^{z/H}\, \mathrm{e}^{-\left(\frac{y-y_0^{up}}{L}\right)^2}, \tag{2}$$

with V_0^{up} the initial velocity of the upwelling jet, $y_0^{up} = L_{\mathrm{domain}}/2$ the latitude of the upwelling jet, and H and L the vertical and zonal extent of the upwelling jet, respectively. This current is then geostrophically adjusted with the density field and the sea surface height. This leads to a temperature front separating cooler waters North from warmer waters South.

In the simulations discussed in this study, we set $V_0^{up} = 0.2\,\mathrm{m\,s^{-1}}$, $H = 200$ m, and $L = 50$ km. These values correspond to those chosen in previous studies (*e.g.* Barth, 1994; Vic et al., 2017) for the study of upwellings.

Sinusoidal perturbation. To trigger the upwelling front instability, we add a sinusoidal perturbation along the front, directly in the initialization of a few experiments. This disturbance idealizes the observed perturbations due to the surrounding flow, or to the atmospheric influence, on the upwelling front. It is usual to choose a single wave as a perturbation in linear, normal-mode theory of flow stability. This disturbance is here a temperature anomaly centered around y_0, and of the form:

$$T_{\text{pert}} = 0.5\,\mathrm{e}^{-z/500}\,\mathrm{e}^{-\left(\frac{y-y_0^{up}}{50\,10^3}\right)^2}\cos\left(\frac{2\pi}{\lambda_{\text{pert}}}\,x\right), \tag{3}$$

with x the zonal direction, and $\lambda_{\text{pert}} = [50,\ 100,\ 250,\ 500,\ 1000]$ km. Varying the wavelength allows the determination of the fastest growing disturbance. The choice of a perturbation deeper than the mean flow is motivated by the likeliness that it is triggered by neighboring currents which are deeper than the upwelling: vortices, or marginal sea outflow currents, or baroclinic Rossby waves. A density anomaly is then computed assuming that the perturbation has no signature in salinity. The velocity field associated with this density anomaly is then obtained *via* the thermal wind balance.

Vortex. To address the main objective of this article (the interaction of an upwelling front with a pre-existing vortex field), we initialize one or several surface-intensified vortices, South of the upwelling front (offshore), in the vortex-front interaction simulations. When several vortices are initialized, they are aligned along the coast offshore of the front. These vortices are initialized in azimuthal velocity (or in vorticity) as in de Marez et al. (2020a,c). For each vortex, we set the initial profile of surface vertical vorticity:

$$\omega(r) = \pm\omega_0\, e^{-\left(\frac{r}{R}\right)^{\alpha}}, \tag{4}$$

with the sign depending on the vortex polarity, $r = \sqrt{(x-x_c)^2 + (y-y_c)^2}$ the radial coordinate referenced at the center of the vortex (x_c, y_c), and α (usually an integer) the steepness parameter.

The surface azimuthal velocity of the vortex can be computed using $v_\theta(r,0) = \frac{1}{r}\int r\,dr\,\omega\,r$. In general it takes the complicated form $v_\theta(r) = (\omega_0 R^2/(\alpha r))\,\gamma((2/\alpha),(r/R)^\alpha)$, where $\gamma(s,x)$ is the incomplete gamma function. In the well-known case of a Gaussian vertical vorticity, with $\alpha = 2$, the azimuthal velocity is $v_\theta(r) = \omega_0 \frac{R^2}{r}\,[1 - e^{-r^2/R^2}]$. In this case, this velocity grows linearly with r, for $r \ll R$, similarly to Rankine vortices. Far from the center, it decays at best as $1/r$ (that is, slower than for a Rankine vortex). To avoid the presence of spurious velocity at the edges of the domain, we apply a Hanning window on v_θ to make it smoothly tend to zero at $r > 3\,R$. The horizontal velocity decreases at depth such that $v_\theta(x,y,z) = v_\theta(x,y,0)\,e^{-z/H_{\text{vortex}}}$, thus defining the height of the vortex H_{vortex}. We de-note (u, v) the horizontal Cartesian components of the velocity of the vortex. The pressure anomaly field $P'(x, y, z)$ corresponding to this velocity field is computed *via* the gradient wind equation:

$$2J(u, v) + f(\partial_x v - \partial_y u) = \frac{1}{\rho}\Delta_h P', \quad (5)$$

with $J(u, v) = \partial_x u \partial_y v - \partial_y u \partial_x v$ the Jacobian operator, and Δ_h the horizontal Laplacian operator. From P' we determine the density and the temperature anomalies of the vortex. These anomalies are computed for as many vortices as we want, at positions x_c, and y_c. Note that such vortices are robust during the whole simulation.

We set $H_{\mathrm{vortex}} = 1000$ m, as surface-intensified vortices are mostly about 1000 m deep in this part of the ocean (Chaigneau et al., 2011; Pegliasco et al., 2015; Keppler et al., 2018; de Marez et al., 2019), and α =24, so that the vortex has a profile close to a Rankine vortex (also called a top-hat vortex, as in *e.g.* de Marez et al. (2020c)). For our study, we vary other initial parameters as R = [50, 100] km, and V_0^{vortex} = [0.2, 0.4, 0.6] $\mathrm{m\,s^{-1}}$ for both cyclonic and anticyclonic vortices. For each set of parameters, we also vary the initial distance between the vortices and the upwelling front as d/R = [2.0, 3.0, 4.0, 5.0], thus setting y_c.

In simulations with an isolated vortex, we set $x_c = L_{\mathrm{domain}}/2$. For simulations with a zonal vortex alley (*i.e.* an alley of vortices of alternated polarities, at a given latitude, with a constant spacing between their centers) we also vary the distance between each vortex d_{btw}/R = [2.0, 3.0, 4.0] and the number of vortices N = [2, 4, 6]. In these cases, the center (in the zonal direction) of the vortex alley is at the center of the domain $L_{\mathrm{domain}}/2$. Therefore $L_{\mathrm{domain}} = N \times d_{\mathrm{btw}}$.

A summary of the three kinds of simulations we ran, with the different parameters we varied, is shown in Fig. 2.

2.2. Diagnostics

2.2.1. Modal decomposition

To analyse the growth of perturbations on the upwelling front, we decompose its deviation from a straight front in zonal Fourier series. We apply this analysis to the surface temperature field at each time step

$$T(x,y) - < T(y) > = \sum_{j=0}^{j=\infty} [c_j(y)\cos(jx) + s_j(y)\sin(jx)] \tag{6}$$

where $< T(y) >$ is the straight temperature front corresponding to $u^{up}(y, z = 0)$. Then, to examine only the modes of the upwelling front, we average c_j and s_j in a 100 km wide meridional band. This gives the time varying amplitude of each mode $\langle c_j^2 + s_j^2 \rangle_y(t)$. In the following, we present and discuss the wavelength of each mode $\lambda = L_{\text{domain}}/j$, with L_{domain} the size of the domain (2000 km).

2.3. The frontogenesis function

To characterize the evolution of buoyancy gradients, we calculate the frontogenesis function F associated with the buoyancy. It is defined as follows (Hoskins, 1982):

$$F(\mathbf{u}, b) = \partial_x u(\partial_x b)^2 + (\partial_x v + \partial_y u)\partial_x b \partial_y b + \partial_y v(\partial_y b)^2.$$

The opposite of the function F indicates the tendency of the buoyancy gradients to steepen:

$$-F(\mathbf{u}, b) = \frac{d}{dt}|\nabla b|^2.$$

2.4. Particle advection

We ran particle advection simulations, using the outputs of CROCO simulations, with the set of python classes Parcels (Parcels stands for “Probably A Really Computationally Efficient Lagrangian Simulator”). This software simulates the advection of an ensemble of particles, using a given 2D or 3D velocity field. This tool has been widely used in the past few years, and it is fully described in Lange & van Sebille (2017); Delandmeter & van Sebille (2019) and in references therein.

The surface velocity field is used here, and the forward advection is computed with a fourth order Runge-Kutta scheme (time spacing $dt = 5$ minutes). Particles are initially set at t =0 days on a regular grid, at $100 \leq x \leq 1900$ km and $500 \leq y \leq 1500$ km, with a spacing between particles of 25 km. Thereby, a total of 2993 particles are advected, throughout the year of simulation.

3. Analysis of the upwelling front instability

3.1. Modal analysis of growing perturbations

Firstly we studied the instability of the straight upwelling front alone (in the absence of any initial vortex). Only a sinusoidal perturbation was added along the front, to trigger its instability (see section 2.1.2 and Fig. 2(left)). The modal amplitude of the growing perturbations (the unstable waves on the front) for various perturbation wavelengths, when one neglects the β-effect (*i.e.* on the f-plane), is shown in Fig. 3(a). We distinguish the time series of amplitudes for a mode with a given wavelength initially (λ_{pert}), from those for the mode which is finally the most unstable one (λ_{max}), and has this wavelength (see also figure caption). If the initial wave grows the fastest, then λ_{pert}=λ_{max}.

When they are forced initially, waves shorter than the most unstable one flso grow but decay rapidly; thus they do not reach large amplitudes. They dominate at short time for fast jets and may thus be related to horizontal shear flow instability. On the contrary, longer waves reach larger amplitudes with time, either within a month or within 8 months. In particular, waves with 200-250 km wavelength are the most unstable over a 1-3 months period; they are followed in amplitude by 500 km long waves. With an internal radius of deformation close to 50-60 km in this oceanic region (Chelton et al., 1998), a wavelength of $2\pi R_d$ = 300-350 km is characteristic of baroclinic instability. Therefore, the growth of these long waves in the first months of simulation can be related to the development of baroclinic instability along the jet. When long waves grow after a longer period (*e.g.* 8 months), their origin is rather to be searched in wave-wave interaction, since the flow is not forced.

A similar modal analysis but now including the β-effect is shown in Fig. 4(a). The β-effect renders flows zonal so that long waves are damped (see *e.g.* Flierl et al. (1999), or the well-known Phillips model of baroclinic instability (Vallis, 2017)). As a result, the most unstable waves in our simulations lie near $\sim$100 km wavelength. In fact, the dimensionless value of β is $\beta L^2/U = L^2/L^2_{\mathrm{Rhines}}$. For the same geophysical value of $\beta = 2 \times 10^{-11}\,\mathrm{m}^{-1}\,\mathrm{s}^{-1}$, this damping effect will be weak for a fast jet such as the Gulf Stream ($U = 1\,\mathrm{m\,s}^{-1}$), but stronger for the jet associated with a typical upwelling front (in our simulations, $U = 0.2\,\mathrm{m\,s}^{-1}$). Therefore meanders on the upwelling front are expected to have a shorter wavelength than those of intense jets such as western boundary currents.

3.2. *Spatial structure of the front with growing perturbations*

3.2.1. *In the absence of β-effect*

When short waves are forced initially, they can grow even if they are shorter than the linearly most unstable wave. This growth will only be transient. These short waves saturate in amplitude without breaking and then slowly decay. Longer waves break and form vortices of about 200 km diameter (see Fig. 3(b)). We note that northward extending (anticyclonic) meanders do not form vortices while southward (cyclonic) meanders do. This North-South asymmetry of meanders on a front can be explained by (1) the difference in local deformation radius (smaller to the North than to the South, if the upper ocean layer is thinner to the North); for baroclinic instability, a smaller deformation radius favors the growth of shorter waves (and conversely); and (2) the curvature vorticity $V/r\ \partial_r V$, which contrary to the geostrophic vorticity is parity biased (here V is the jet velocity magnitude in the meander, and r is the radius of curvature of the meander). These arguments can explain the growth of longer waves than those initialized, South of the jet, thus leading to the breaking of meanders into vortices. Such asymmetries do not appear in quasi-geostrophic simulations of jet instability.

The most unstable wave is determined by computing its growth during the early stage of the evolution. When this wave is initialized (*e.g.* $\lambda_{\rm pert} = 250$ km), it grows up to breaking the front, generating vortices of $\sim$200 km diameter. Since the most unstable perturbation is initialized everywhere, vortices form both north and south of the jet. Along the central latitude, the jet comes back to a quasi zonal state once the vortices have detached. This effect has been explained in previous studies (Baey et al., 1999) and it can be clearly seen on Fig. 3(c).

If a longer wave is initialized, shorter waves emerge *via* nonlinear wave-wave interactions, and finally vortices of $\sim$200 km diameter form. These nonlinear wave interactions also generate other features such as filaments and smaller vortices (see Fig. 3(d)).

3.2.2. *In the presence of β-effect*

When β-effect is added, long waves do not grow and shorter waves dominate the evolution of the flow. This leads to the generation of filaments and of small vortices (of $\sim$50 km diameter). The most unstable wave form vortices of $\sim$100 km diameter. Since the β-effect renders flows zonal, meanders grow less north and south, and the perturbations remain confined near the front axis, see Fig. 4(b,c,d). Even long waves imposed initially on the front bifurcate towards smaller meanders. Still, they do not form very small scale features and thus the flow pattern is spatially more regular.

4. Upwelling front evolution in the presence of a single vortex

Now that the instability of the front, without external vortex, has been studied, we investigate the influence of a single vortex on this same front. The vortex is initialized south of the front and it replaces the perturbation added to the front in the previous section (see section 2.1.2 and Fig. 2(middle)). This vortex deforms the front along its own spinning motion. Here, we do not perform a Fourier analysis of the front perturbation; indeed, the wavelength which is the most unstable on the straight front in the absence of external vortex, is now perturbed by the presence of the vortex. Performing this analysis here would in particular reflect the vortex size. For the simulations discussed here, the vortex position, polarity, radius, and velocity are varied. The evolution of the front on the f-plane and on the β-plane is now presented. The position of the front is chosen as the isotherm corresponding to the average of the northern and southern temperature after 100 (resp. 200) days of simulated time in Fig. 5 (resp. Fig. 6).

4.1. The reference cases

To further study the influence of the vortex parameters on the front stability, we define reference cases, for which the vortex can have either polarity, a radius $R = 100$ km (corresponding to the radius of vortices formed by the instability of the front previously described), a distance to the front $d = 2R$, and an azimuthal velocity $V_0^{\text{vortex}} = \pm 0.2\,\mathrm{m\,s^{-1}}$ initially. The front positions in these cases are shown by solid color lines in Figs. 5 and 6.

In this case, on the f-plane, the presence of a vortex south of the front induces a meridional deformation of the front in its vicinity, but not over the whole length of the domain, during the first three months of simulation. At later times (200 days), this filament extrudes offshore and detaches from the front. Also, the most unstable wave of the front grows, leading to small scale perturbations along the whole front.

After 3 months, we observe that if the vortex is cyclonic, the front is more deformed than if the vortex were anticyclonic. This can be explained by the following. Though their relative vorticities are initially antisymmetric, their Ertel potential vorticities are asymmetric. Indeed, even at first order beyond quasi-geostrophy the absolute vorticity multiplies the density anomaly, and we can write this first-order Ertel potential vorticity anomaly as

$$\delta Q = \omega + (f_0 + \omega) b / N^2,$$

where b is the buoyancy anomaly associated with the vortex, and N the Brunt-Väisälä frequency $N^2 = -\frac{\partial b}{\partial z}$. δQ characterizes the vortex ability to remotely influence its environment. Since ω and b are antisymmetric at first order for cyclones and anticyclones, δQ is larger in modulus for cyclones. Again at first order, this potential vorticity anomaly is conserved in time. Stern & Flierl (1987) have shown that in two-dimensional flows, a vorticity front develops a meander with equal and opposite circulation to that of the vortex deforming it. Applying this principle here explains why fronts extrude longer and/or larger filaments when nearing a cyclone than an anticyclone; this can be seen after 100 simulated days. After 200 days, the perturbation breaks down non-linearly and becomes spatially more convoluted and intricate. These nonlinear effects can also lead to the production of long offshore filaments by fronts under the influence of anticyclones, but this effect is weaker than after 100 days. Meanders and filaments are much smaller in the presence of β-effect than in its absence.

4.2. Sensitivity to the vortex radius

The influence of the vortex radius R on the flow evolution is studied for a vortex lying at a distance $d = 2R$ from the front, with an azimuthal velocity $V_0^{\mathrm{vortex}} = \pm 0.2\,\mathrm{m\,s^{-1}}$ initially, see Figs. 5(a,b) and 6(a,b). Under these conditions, wider vortices lead to longer filaments offshore both after 100 and 200 days. On the f-plane, smaller vortices yield more wave amplification downstream, and in particular more coastal intrusion of open ocean fluid (*i.e* South of the front). The growth of a longer filament in the presence of a larger vortex is also associated with a weaker growth of the 200 km long wave on the front; the evolution of the front under the influence of the vortex supersedes the unstable evolution of the front (alone).

At long times, the long frontal wave recovers its strength of the jet instability case, for both small and large vortices. In the presence of β-effect, cyclonic vortices drift northwestward and thus come closer to the front while anticyclonic vortices drift away from the front on the β-plane, explaining the difference in the generated filament lengths. Again, the zonal straightening effect of β on streamlines prevails, so that shorter filaments are generated on the β-plane than on the f-plane.

4.3. Sensitivity to the vortex intensity

The influence of the vortex intensity V_0^{vortex} is studied for a vortex lying at a distance $d = 2R$ from the front, with a radius $R = 100$ km initially, see Figs. 5(c,d) and 6(c,d). When V_0^{vortex} increases, so does the vortex dynamical influence on the front. Thus, the filaments growing from the front increase in size.

On the f-plane, after 100 days, the filaments wrap up around the vortex. Though the perturbation is concentrated around the quasi-steady vortex, this interaction leads to much offshore export of coastal fluid. Again, cyclones disturb the front more deeply than anticyclones do. After 200 days, filaments still protrude far offshore on the f-plane, but forced waves have now propagated along the front axis so that much offshore-coastal fluid exchange occurs, all along the front axis.

On the β-plane, short waves develop on the front, with smaller amplitude than on the f-plane. The most intense external vortices induce more small scale turbulent features. Again, more small-scale features are induced by cyclones than by anticyclones. After 100 days, these small-scale features remain trapped between the front and the vortex and do not drift far offshore. This can be related to the flow straightening by the β-effect, and to the westward vortex drift which, for the front and its meanders, displaces the external deformation field. After 200 days, turbulence has developed from its state at 100 days. It extends all along the front and the inshore-offshore fluid exchange is amplified. Still, no coastal fluid is advected offshore beyond the vortex. Here, the meridional gradient of upper layer vortex stretching (across the front) is positive, which increases the westward Rossby wave speed so that frontal meanders are located more to the West than on the f-plane.

4.4. Sensitivity to the vortex distance to the front

The influence of the distance between the vortex and the front d/R is studied for a vortex with a radius $R = 100$ km, and an azimuthal velocity $V_0^{\mathrm{vortex}} = \pm 0.2\,\mathrm{m\,s^{-1}}$ initially, see Figs. 5(e,f) and 6(e,f). The same observations as in the previous subsection hold here. On the f-plane, after 100 days, long waves grow and large meanders break into offshore filaments when the vortex is close to the front (d/R =2 or 3). After 200 days, shorter waves develop and affect the whole length of the front. Here again, cyclones induce more pronounced deformations and longer filaments than anticyclones. When $d/R = 4$ or 5, very little deformation of the front occurs, both on the f- and on the β-plane. As a consequence, vortices lying 400 km away from the upwelling front influence it very little, as could be anticipated from the calculation of the velocity field. On the β-plane, the stabilizing effect of the planetary vorticity gradient confines the waves and the turbulence to the vicinity of the front.

5. Interaction of an upwelling front with a vortex alley

Though the interaction of a single vortex with an upwelling front is an important step in our study, and though analyzing this case provides important and general conclusions, sea surface measurements in the Arabian Sea show that the southern Omani upwelling is rarely bordered by only one vortex; multiple vortices surround the front (see *e.g.* Fig. 1). Therefore, we generalize the previous case to that of a vortex alley along the front (see section 2.1.2 and Fig. 2(right)). We use the physical vortex parameters of the most significant case previously analyzed: $V_0^{\mathrm{vortex}} = 0.2\,\mathrm{m\,s^{-1}}$, $R = 100$ km, and $d/R = 2$. Here we vary the alongshore distance between the vortices d_{btw}, the number of vortices N, and the presence or absence of β-effect.

5.1. Sensitivity to the number of vortices

We present the case with $d_{\mathrm{btw}}/R = 4$, which shows the highest efficiency for filament production, for $N = 2 - 6$ vortices, see Figs. 7(a,b) and 8(a,b). On the f-plane, at $t = 100$ days, the effect for each vortex is comparable to that of a single vortex, *i.e.* long filaments protrude offshore from the front. The velocity field field resulting from the addition of the vortices is stronger at the center of the domain, and thus the filaments are longer there. Filaments are advected southward between an anticyclone (to the West) and a cyclone (to the East). On the contrary, the front is pushed northwards and forms a wide meander to the North, between a cyclone (to the West) and an anticyclone (to the East). At $t = 200$ days, the filaments have been cut, and some of them are brought closer to the front by the velocity field of the zonal jet. We can also see (as in the reference cases, see section 4.1), the development of shorter waves, which now grow on the wide meanders. This state is comparable to that of the nonlinear evolution of the unstable front in the absence of external vortices initially. Note a difference between the present case and that with a single external vortex: here, the front is shifted North, which did not occur with only one vortex. On the β-plane, again, shorter and less prominent meanders and filaments are produced after 100 days. These waves break into a turbulent field, in the vicinity of the front, after 200 days.

5.2. Sensitivity to the distance between vortices

The influence of the distance between vortices within the vortex alley $d_{\rm btw}/R$ is studied for a vortex alley of 6 vortices (*i.e.* N=6, this corresponds to cases with the most intense deformation of the front), see Figs. 7(c,d) and 8(c,d). We do not detail each figure individually, but we note that for short times, the larger the inter-vortex distance is, the stronger the offshore mass transport is. Indeed, the alongshore extent of the front deformation and the filament widths increase with $d_{\rm btw}$. At longer time, the northward displacement of the front is larger for small $d_{\rm btw}$ because the vorticity dipoles which are generated are more intense (the distance between the centers of the two vortices in the dipole being smaller). On the contrary, on the β-plane, the front show more long wave (200 km length) instability when $d_{\rm btw}$ is larger (the vortices triggering longer waves). Again, the β-effect reduces the amplitude of meanders and intensifies turbulence in the vicinity of the front.

6. Discussion: cross-shore exchange of particles

We discuss here the impact of vortices and of upwelling destabilization on the transport of fluid particles in the domain. In particular, we present the export and import of particles across the y-position of the upwelling, to assess the role of the different dynamical elements in the particle transport off-shore (from North to South) and on-shore (from South to North). This point is key to the local dynamics of upwelling rich regions because this can trigger phytoplankton blooms (Shi et al., 2000; Liao et al., 2016).

To do so, we ran particle advection simulations (see details in section 2.4) in 4 particular CROCO simulations, which are the most representative of the upwelling-vortex interactions behavior. For further use, we define onshore as shorewards of the front (*i.e.* North of the front), and offshore conversely. The particle evolution with time is presented for an upwelling front with a sinusoidal perturbation (a), in the presence of a cyclone (b), of an anticyclone (c), or of a vortex alley (d), on the f-plane (Fig. 9) or on the β-plane (Fig. 10).

For the perturbed front, the particles drift onshore and offshore nearly equally on the f-plane, while the cross-shore exchange is strongly reduced on the β-plane (as expected). When the front faces a single cyclone, on the f-plane, offshore particles are trapped in a meander which wraps counterclockwise and shore-ward, after 100 days. After 200 days, this meander undergoes instability and produces shorter scale meanders; it breaks and gives birth to many small vortices inshore of the front. The offshore meander at 100 days produces a long-wave perturbation on the front, leading to the offshore motion of onshore particles. This meander also breaks into smaller fragments (small vortices and filaments). Such fragments are seen on Chlorophyll-a images of the Oman upwelling front (such an image can be found in lecture 17 of Lisa Beal's oceanography course: https://beal-agulhas.rsmas.miami.edu/teaching/courses/lecture-seventeen/index.html). On the β-plane, the cross-shore displacement of particles, and their meridional flux, are strongly reduced, but small-scale patches of displaced particles are still present on both sides of the front. When the front faces an anticyclone on the f-plane, a large meander of coastal water is pulled offshore and carries passive particles across the front after 100 days. This meander breaks into a coherent, medium scale cyclone, next to the anticyclone. After 360 days, both the vortex interactions and the front breaking lead to the production of small-scale filaments and vortices offshore. This phenomenon is considerably weakened on the β-plane where only three small vortices containing coastal water are found offshore after 200 days. After 360 days, particles have been displaced inside the offshore region, but little cross-front exchange has taken place. In the presence of a vortex row, on the f-plane, the intrusion and extrusion of fluid *via* the front meanders and the subsequent filaments lead to substantial cross-front exchange, in particular *via* small-scale features. On the β-plane, the cross-front flux is still the largest of all simulations, visually.

The median particle export distance for each case, in the onshore and offshore direction, and the percentage of exported particles are shown in Fig. 11. On the f-plane, the front with a vortex alley or with a cyclone displace more particles than the unstable front or the front with an anticyclone, but the front with a cyclone advects particles only close to the front. On the β-plane, much fewer particles are advected across the front and the export distance is strongly reduced. Again, the front with a cyclone or with a vortex alley advect more particles. The latter case is the most efficient to horizontally stir particles. Finally, the frontogenesis function computed in the front-vortex alley case (Fig. 12) indicates that frontogenetic tendency is large around the small vortices and formed filaments.

For a comparison of these results with the upwelling and vortices off Oman (see Fig. 1), we can see that the cyclone lying offshore of the front (at 17°N, 57°E) pulls a long filament away from the front. On the SST map (Fig. 1(a)) cold water extends offshore at least over 300 km. South of the main cyclone, a smaller cyclone, containing cold water, is found. Another filament, shorter than the former, is torn away from the upwelling front by the anticyclone lying at 20°N and 60°E. On the SST and SSH maps, contrary to our model, more vortices lie farther offshore of those close to the front. They also carry cold water away from the coast and make it recirculate.

These results suggest that the impacts of upwelling front instability or front interaction with a vortex field on biological activity are expected to be important. Firstly, nutrient rich onshore waters will be exported offshore by the meanders which then break into filaments and into small vortices. These flow structures will be the seat of intense biological activity (blooms) favored by the further vertical uplift of nutrients to the surface, related to frontogenesis. Secondly, exchange of coastal and deep water species will be achieved by these horizontal exchanges, leading to a possible modification of local ecosystems, and to possible competitive exclusion of species, in an otherwise protected environment for them.

7. Conclusions

We have studied the evolution of an unstable upwelling front and of a front in the presence of vortices offshore. We have not considered a stable front in the presence of external vortices, because upwelling fronts are naturally unstable. The characteristic wavelengths and coherent structures produced by these evolutions have been determined. Their impact in terms of horizontal fluxes of particles has been studied. In particular, wavelengths of 100 or 200 km appear on the front, and small-scale filaments and vortices are finally produced. Frontogenesis is strong around them. Mesoscale vortices and smaller scale features advect particles across the front. The timescales of 3-6 months considered here can be made shorter by considering faster frontal currents (*e.g.* in the linear approximation, a 0.4-1 $\mathrm{m\,s^{-1}}$ frontal jet will reduce the timescales by factors of 2 to 5, leading to periods of about 1 month for the formation of meanders and filaments). Numerical simulations using particles advection have shown that a vortex alley is the most efficient perturbation to the upwelling front, in terms of cross-front transport (compared with a single vortex, or with the instability of the front alone).

Still, this study remains idealized in terms of flow conditions. First and foremost, it has only considered the inertial (unforced) evolution of the front. We will extend these results in a following study by adding wind stress and/or the front relaxation to a prescribed state, to assess the energetic balance between atmospheric forcing and mean flow instability. Bottom topography and coastal irregularities should also be added as they can alter or favor the formation of filaments and of vortices from upwelling fronts (Meunier et al., 2010). The wind variability is also essential in the evolution of upwelling fronts, by either weakening them or amplifying them. Further studies with nested models of the Arabian Sea and of the region south of Oman will be done in the near future. They will benefit from *in situ* measurements performed during the Physindien 2019 experiment South of the Sultanate of Oman, for their validation.

Participation in the study

The authors declare their participation in the study, CdM for conception, numerical work and contribution to the paper writing, XC for conception, participation in the analyses and paper writing. The authors declare no conflict of interest in the realization of this work.

Acknowledgments

This work was funded by the Direction Générale de l'Armement (DGA) *via* a full grant for Charly de Marez's PhD. This work is also a contribution to PRC 1069 'Meso and submesoscale vortices in the Atlantic and Indian Ocean', funded by CNRS and RFBR. Simulations were performed using the HPC facilities DATARMOR of "Pôle de Calcul Intensif pour la Mer" at Ifremer, Brest, France. Model outputs are available upon request.

References

Al Saafani, M. A., Shenoi, S. S. C., Shankar, D., Aparna, M., Kurian, J., Durand, F., & Vinayachandran, P. N. (2007). Westward movement of eddies into the Gulf of Aden from the Arabian Sea. *Journal of Geophysical Research*, *112*, C11004. doi:10.1029/2006JC004020.

Ayouche, A., De Marez, C., Morvan, M., L'Hégaret, P., Carton, X., Le Vu, B., & Stegner, A. (2021). Structure and dynamics of the Ras al Hadd oceanic dipole in the arabian sea. In *Oceans* (pp. 105–125). Multidisciplinary Digital Publishing Institute volume 2.

Baey, J.-M., Riviere, P., & Carton, X. (1999). Ocean jet instability: a model comparison. *ESAIM: Proceedings*, *7*, 12–23. doi:10.1051/proc:1999013.

Barth, J. A. (1994). Short-wave length instabilities on coastal jets and fronts. *Journal of Geophysical Research*, *99*, 16095. doi:10.1029/94JC01270.

Brandt, P., Stramma, L., Schott, F., Fischer, J., Dengler, M., & Quadfasel, D. (2002). Annual Rossby waves in the Arabian Sea from TOPEX/POSEIDON altimeter and in situ data. *Deep Sea Research Part II: Topical Studies in Oceanography*, *49*, 1197–1210. doi:10.1016/S0967-0645(01)00166-7.

Bruce, J. (1974). Some details of upwelling off the somali and arabian coasts, .

Bruce, J. G., Johnson, D. R., & Kindle, J. C. (1994). Evidence for eddy formation in the eastern Arabian Sea during the northeast monsoon. *Journal of Geophysical Research*, *99*, 7651. doi:10.1029/94JC00035.

Capet, X. J., & Carton, X. J. (2004). Nonlinear regimes of baroclinic boundary currents. *Journal of Physical Oceanography*, *34*, 1400 – 1409.

Chaigneau, A., Le Texier, M., Eldin, G., Grados, C., & Pizarro, O. (2011). Vertical structure of mesoscale eddies in the eastern South Pacific Ocean: A composite analysis from altimetry and Argo profiling floats. *Journal of Geophysical Research*, *116*. doi:10.1029/2011JC007134.

Chelton, D. B., deSzoeke, R. A., Schlax, M. G., El Naggar, K., & Siwertz, N. (1998). Geographical Variability of the First Baroclinic Rossby Radius of Deformation. *Journal of Physical Oceanography*, *28*, 433–460. doi:10.1175/1520-0485(1998)028<0433:GVOTFB>2.0.CO;2.

Csanady, G. T. (1982). On the structure of transient upwelling events. *Journal of Physical Oceanography*, *12*, 84 – 96.

Currie, R. (1992). Circulation and upwelling off the coast of south-east arabia. *Oceanologica Acta*, *15*, 43–60.

Delandmeter, P., & van Sebille, E. (2019). The Parcels v2.0 Lagrangian framework: new field interpolation schemes. *Geoscientific Model Development*, *12*, 3571–3584. doi:10.5194/gmd-12-3571-2019.

Elliott, A. J., & Savidge, G. (1990). Some features of the upwelling off Oman. *Journal of Marine Research*, *48*, 319–333. doi:10.1357/002224090784988764.

Fischer, A. S., Weller, R. A., Rudnick, D. L., Eriksen, C. C., Lee, C. M., Brink, K. H., Fox, C. A., & Leben, R. R. (2002). Mesoscale eddies, coastal upwelling, and the upper-ocean heat budget in the Arabian Sea. *Deep Sea Research Part II: Topical Studies in Oceanography*, *49*, 2231–2264. doi:10.1016/S0967-0645(02)00036-X.

Flierl, G. R., Carton, X. J., & Messager, C. (1999). Vortex formation by unstable oceanic jets. *ESAIM: Proceedings*, *7*, 137–150. doi:10.1051/proc:1999013.

Hidaka, K. (1972). Physical oceanography of upwelling. *Geoforum*, *3*, 9–21. doi:10.1016/0016-7185(72)90082-6.

Hoskins, B. (1982). The mathematical theory of frontogenesis. *Annual review of fluid mechanics*, *14*, 131–151. doi:10.1146/annurev.fl.14.010182.001023.

Keppler, L., Cravatte, S., Chaigneau, A., Pegliasco, C., Gourdeau, L., & Singh, A. (2018). Observed Characteristics and Vertical Structure of Mesoscale Eddies in the Southwest

Tropical Pacific. *Journal of Geophysical Research: Oceans*, *123*, 2731–2756. doi:10.1002/2017JC013712.

Klein, P., Hua, B. L., Lapeyre, G., Capet, X., Le Gentil, S., & Sasaki, H. (2008). Upper ocean turbulence from high-resolution 3D simulations. *J. Phys. Oceanogr.*, *38*, 1748–1763.

Lange, M., & van Sebille, E. (2017). Parcels v0.9: prototyping a Lagrangian ocean analysis framework for the petascale age. *Geoscientific Model Development*, *10*, 4175–4186. doi:10.5194/gmd-10-4175-2017.

Large, W. G., McWilliams, J. C., & Doney, S. C. (1994). Oceanic vertical mixing: A review and a model with a nonlocal boundary layer parameterization. *Reviews of Geophysics*, *32*, 363–403. doi:10.1029/94RG01872.

Liao, X., Zhan, H., & Du, Y. (2016). Potential new production in two upwelling regions of the western arabian sea: Estimation and comparison. *Journal of Geophysical Research Oceans*, *121*, 4487–4502. doi:10.1002/2016JC011707.

Manghnani, V., Morrison, J. M., Hopkins, T. S., & Böhm, E. (1998). Advection of upwelled waters in the form of plumes off oman during the southwest monsoon. *Deep Sea Research Part II: Topical Studies in Oceanography*, *45*, 2027–2052. doi:https://doi.org/10.1016/S0967-0645(98)00062-9.

de Marez, C., Carton, X., L'Hégaret, P., Meunier, T., Stegner, A., Le Vu, B., & Morvan, M. (2020a). Oceanic vortex mergers are not isolated but influenced by the β-effect and surrounding eddies. *Scientific Reports*, *10*. doi:10.1038/s41598-020-59800-y.

de Marez, C., L'Hégaret, P., Morvan, M., & Carton, X. (2019). On the 3D structure of eddies in the Arabian Sea. *Deep Sea Research Part I: Oceanographic Research Papers*, . doi:10.1016/j.dsr.2019.06.003.

de Marez, C., Meunier, T., Morvan, M., L'Hegaret, P., & Carton, X. (2020b). Study of the stability of a large realistic cyclonic eddy. *Ocean Modelling*, *146*, 101540. doi:10.1016/j.ocemod.2019.101540.

de Marez, C., Meunier, T., Tedesco, P., L'Hégaret, P., & Carton, X. (2020c). Vortex–wall interaction on the β-plane and the generation of deep submesoscale cyclones by internal Kelvin Waves–current interactions. *Geophysical & Astrophysical Fluid Dynamics*, (pp. 1–19). doi:10.1080/03091929.2020.1772779.

McCreary, J. (1981). A linear stratified ocean model of the coastal undercurrent. *Philosophical Transactions of the Royal Society of London. Series A, Mathematical and Physical Sciences*, *302*, 385–413.

McDougall, T. J., & Barker, P. M. (2011). Getting started with teos-10 and the gibbs seawater (gsw) oceanographic toolbox. *SCOR/IAPSO WG*, *127*, 1–28.

Ménesguen, C., Le Gentil, S., Marchesiello, P., & Ducousso, N. (2018). Destabilization of an oceanic meddy-like vortex: energy transfers and significance of numerical settings. *J. Phys. Oceanogr.*, *48*, 1151–1168. doi:10.1175/jpo-d-17-0126.1.

Meunier, T., Rossi, V., Morel, Y., & Carton, X. (2010). Influence of bottom topography on an upwelling current: Generation of long trapped filaments. *Ocean Modelling*, *35*, 277–303. doi:10.1016/j.ocemod.2010.08.004.

Pedlosky, J. (1974). Longshore currents and the onset of upwelling over bottom slope. *Journal of Physical Oceanography*, *4*, 310–320.

Pedlosky, J. (1978a). An inertial model of steady coastal upwelling. *Journal of Physical Oceanography*, *8*, 171–177.

Pedlosky, J. (1978b). A nonlinear model of the onset of upwelling. *Journal of Physical Oceanography*, *8*, 178–187.

Pegliasco, C., Chaigneau, A., & Morrow, R. (2015). Main eddy vertical structures observed in the four major Eastern Boundary Upwelling Systems. *Journal of Geophysical Research: Oceans*, *120*, 6008–6033. doi:10.1002/2015JC010950.

Piontkovski, S., & Al-Jufaili, S. (2013). Coastal upwellings and mesoscale eddies of the western Arabian Sea: some biological implications. *International Journal of Oceans and Oceanography*, *7*, 93–115.

Pratt, L., & Stern, M. E. (1986). Dynamics of potential vorticity fronts and eddy detachment. *Journal of physical oceanography*, *16*, 1101–1120.

Privett, D. (1959). Monthly charts of evaporation from the N. Indian Ocean (including the Red Sea and the Persian Gulf). *Quarterly Journal of the Royal Meteorological Society*, *85*, 424–428.

Sastry, J., & d'Souza, R. (1972). Upwelling and upward mixing in the Arabian Sea, .

Schott, F. A., & Fischer, J. (2000). Winter monsoon circulation of the northern Arabian Sea and Somali Current. *Journal of Geophysical Research: Oceans*, *105*, 6359–6376. doi:10.1029/1999JC900312.

Shchepetkin, A. F., & McWilliams, J. C. (2005). The regional oceanic modeling system (ROMS): a split-explicit, free-surface, topography-following-coordinate oceanic model. *Ocean Modell.*, *9*, 347–404.

Shchepetkin, A. F., & McWilliams, J. C. (2011). Accurate Boussinesq oceanic modeling with a practical, "stiffened" equation of state. *Ocean Modell.*, *38*, 41–70. doi:10.1016/j.ocemod.2011.01.010.

Shi, W., Morrison, J., Böhm, E., & Manghnani, V. (2000). The Oman upwelling zone during 1993, 1994 and 1995. *Deep Sea Research Part II: Topical Studies in Oceanography*, *47*, 1227–1247. doi:10.1016/S0967-0645(99)00142-3.

Smith, W. H. F., & Sandwell, D. T. (1997). Global Sea Floor Topography from Satellite Altimetry and Ship Depth Soundings. *Science*, *277*, 1956–1962. URL: http://www.sciencemag.org/lookup/doi/10.1126/science.277.5334.1956. doi:10.1126/science.277.5334.1956.

Stern, M. E., & Flierl, G. R. (1987). On the interaction of a vortex with a shear flow. *Journal of Geophysical Research: Oceans*, *92*, 10733–10744.

Suginohara, N. (1977). Upwelling front and two-cell circulation. *Journal of the Oceanographical Society of Japan*, *33*, 115–130.

Trott, C. B., Subrahmanyam, B., Chaigneau, A., & Roman-Stork, H. L. (2019). Eddy-Induced Temperature and Salinity Variability in the Arabian Sea. *Geophysical Research Letters*, *46*, 2734–2742. doi:10.1029/2018GL081605.

Vallis, G. K. (2017). *Atmospheric and oceanic fluid dynamics: fundamentals and large-scale circulation*. Cambridge University Press.

Vandermeirsch, F. O., Carton, X. J., & Morel, Y. G. (2003a). Interaction between an eddy and a zonal jet. *Dynamics of Atmospheres and Oceans*, *36*, 271–296. doi:10.1016/S0377-0265(02)00066-0.

Vandermeirsch, F. O., Carton, X. J., & Morel, Y. G. (2003b). Interaction between an eddy and a zonal jet. *Dynamics of Atmospheres and Oceans*, *36*, 247–270. doi:10.1016/S0377-0265(02)00065-9.

Vic, C., Capet, X., Roullet, G., & Carton, X. (2017). Western boundary upwelling dynamics off Oman. *Ocean Dynamics*, *67*, 585–595. doi:10.1007/s10236-017-1044-5.

Vic, C., Roullet, G., Capet, X., Carton, X., Molemaker, M. J., & Gula, J. (2015). Eddy-topography interactions and the fate of the Persian Gulf Outflow. *Journal of Geophysical Research: Oceans*, *120*, 6700–6717.

Yoshida, K. (1955). Coastal upwelling off the California coast. *Rec. Oceanogr. Works Japan, New Ser.*, *2*, 8–20.

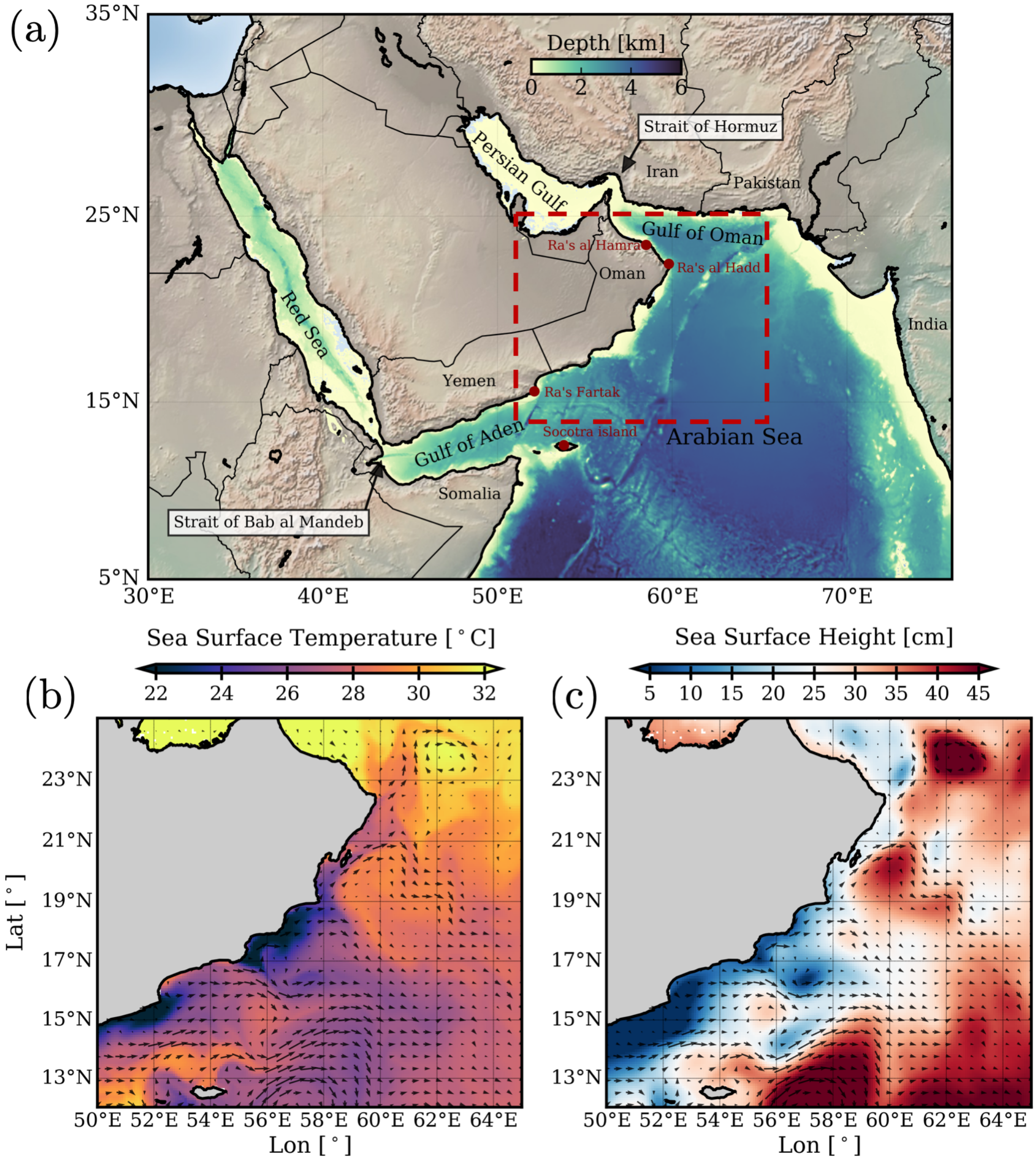

Figure 1: (a) Bathymetry in the Arabian Sea and adjacent gulfs from ETOPO2 (Smith & Sandwell, 1997), dashed rectangle shows the geographic position of panels (b,c). (b) Sea Surface Temperature and (c) Sea Surface Height (SSH) along the Omani coast in the Arabian Sea on 05/08/2020. Arrows show the geostrophic velocity derived from SSH. Cold filaments resulting from the steering of the upwelling by mesoscale eddies are seen near 56°E 16°N. Data are from Operational Mercator global ocean analysis and forecast system (downloaded on Copernicus website).

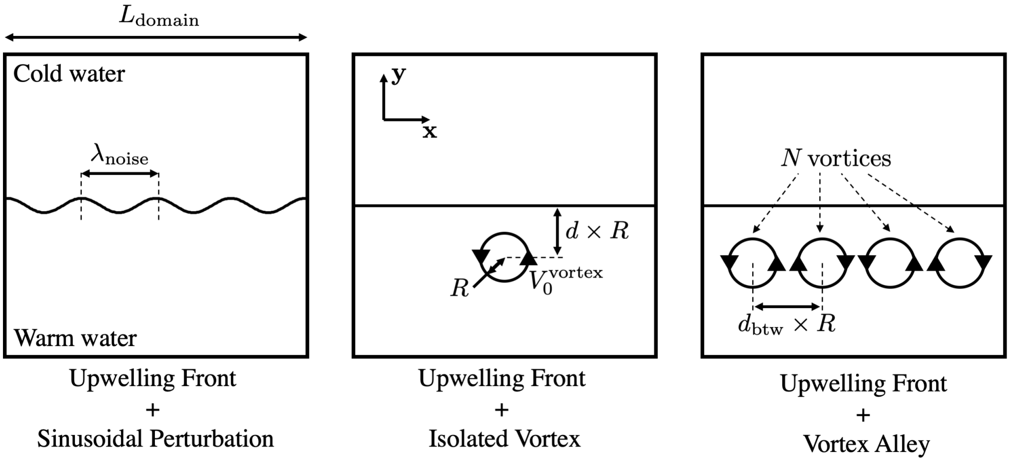

Figure 2: Scheme of the three kinds of simulations we performed and the different physical parameters we varied.

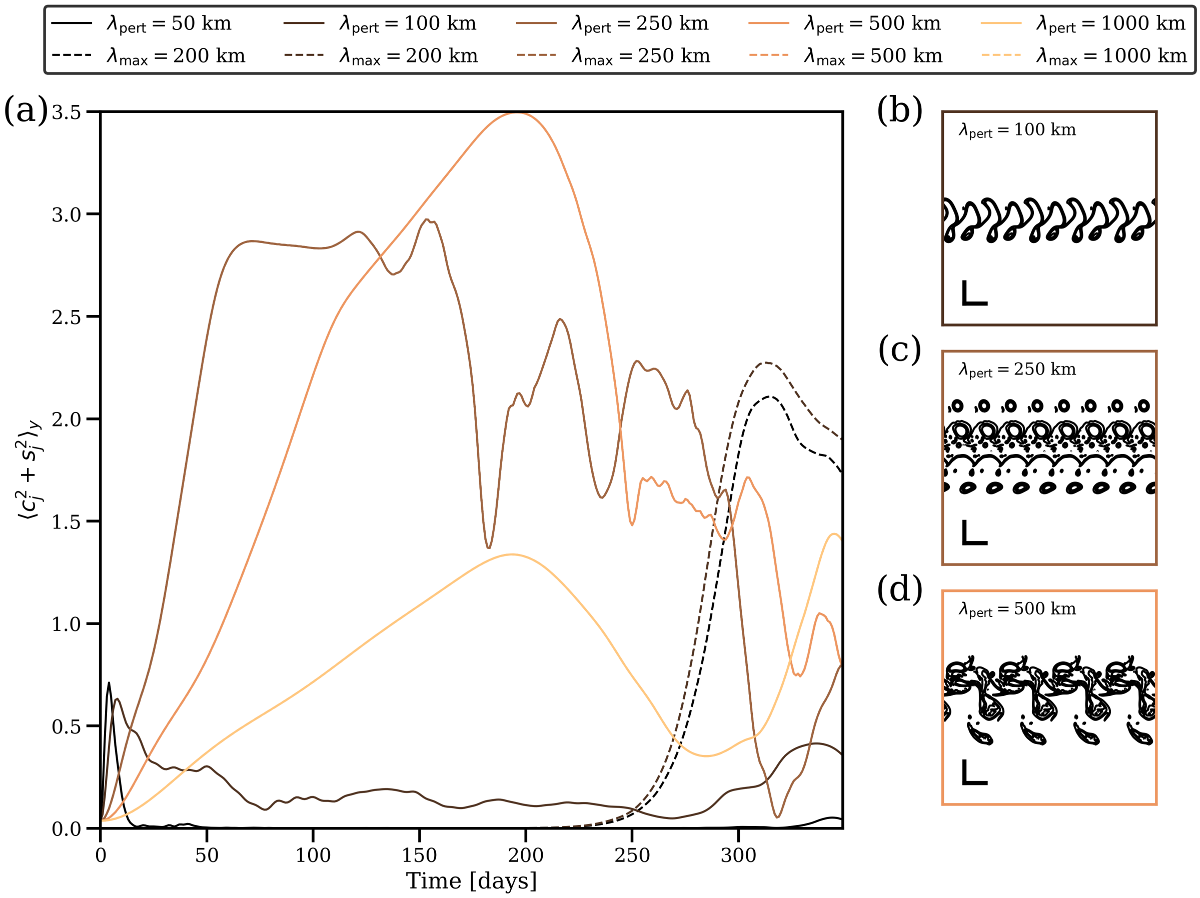

Figure 3: a) Time evolution of the amplitude of modes from the modal decomposition of the surface temperature, in simulations with an upwelling front and an initial sinusoidal perturbation, for $L = 50$ km, $H = 200$ m, and $V_0^{up} = 0.2\,\mathrm{m\,s^{-1}}$. The color of the line indicates the wavelength of the wave at initialization (λ_{pert}), such that one color designate one simulation. Solid lines show the evolution of the mode with the same wavelength as the initial perturbation (λ_{pert}), while dashed lines show the evolution of the mode that reaches the largest amplitude (with a wavelength $\lambda_{\max}$). If the solid and dashed lines are superposed, the mode that reaches the largest amplitude has the same wavelength as the initial perturbation. b),c), and d) Surface temperature contours after one year in the simulations with $L = 50$ km, $H = 200$ m, and $V_O^{up} = 0.2\,\mathrm{m\,s^{-1}}$, and λ_{pert} =100, 250, and 500 km. Sizebars in the bottom left of each panel show a distance of 200×200 km.

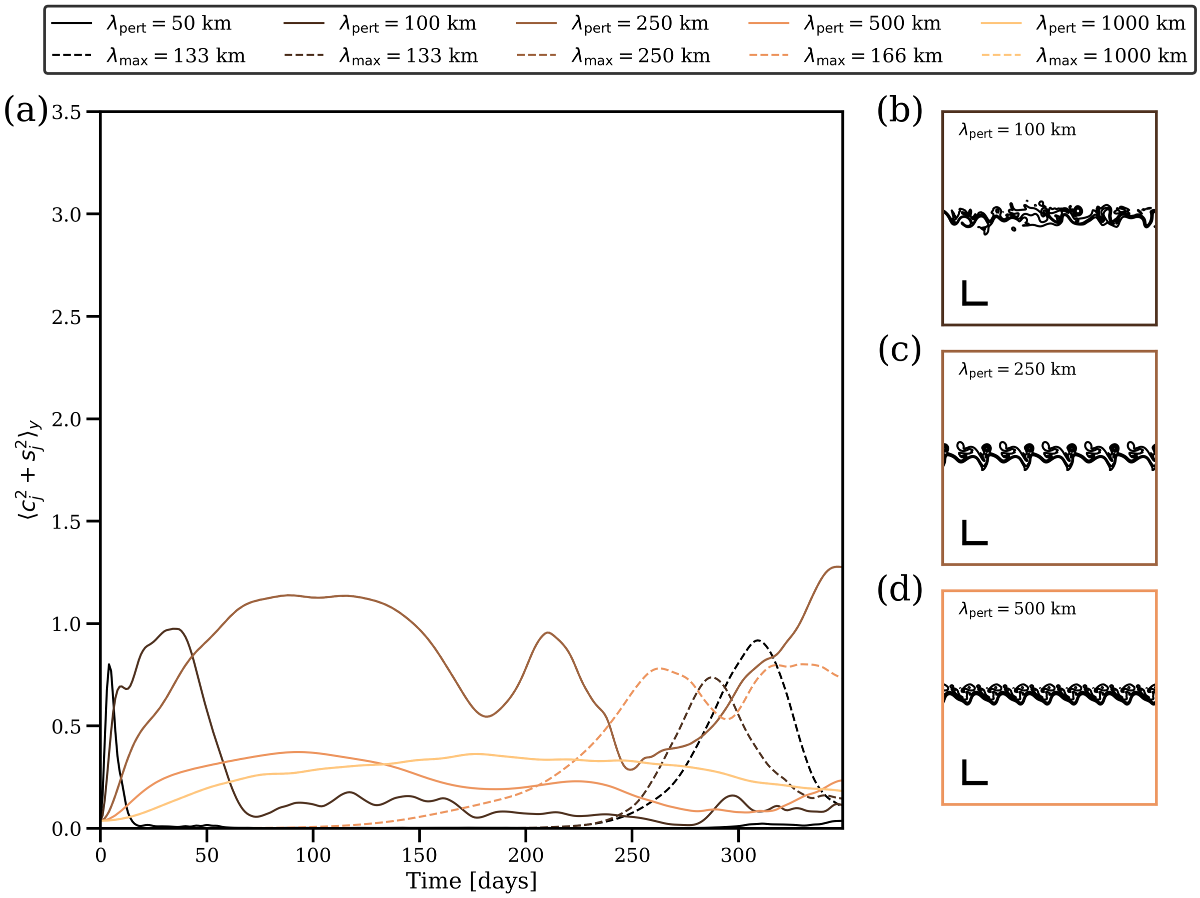

Figure 4: Same as Fig. 3, but with a β-effect added in the simulation.

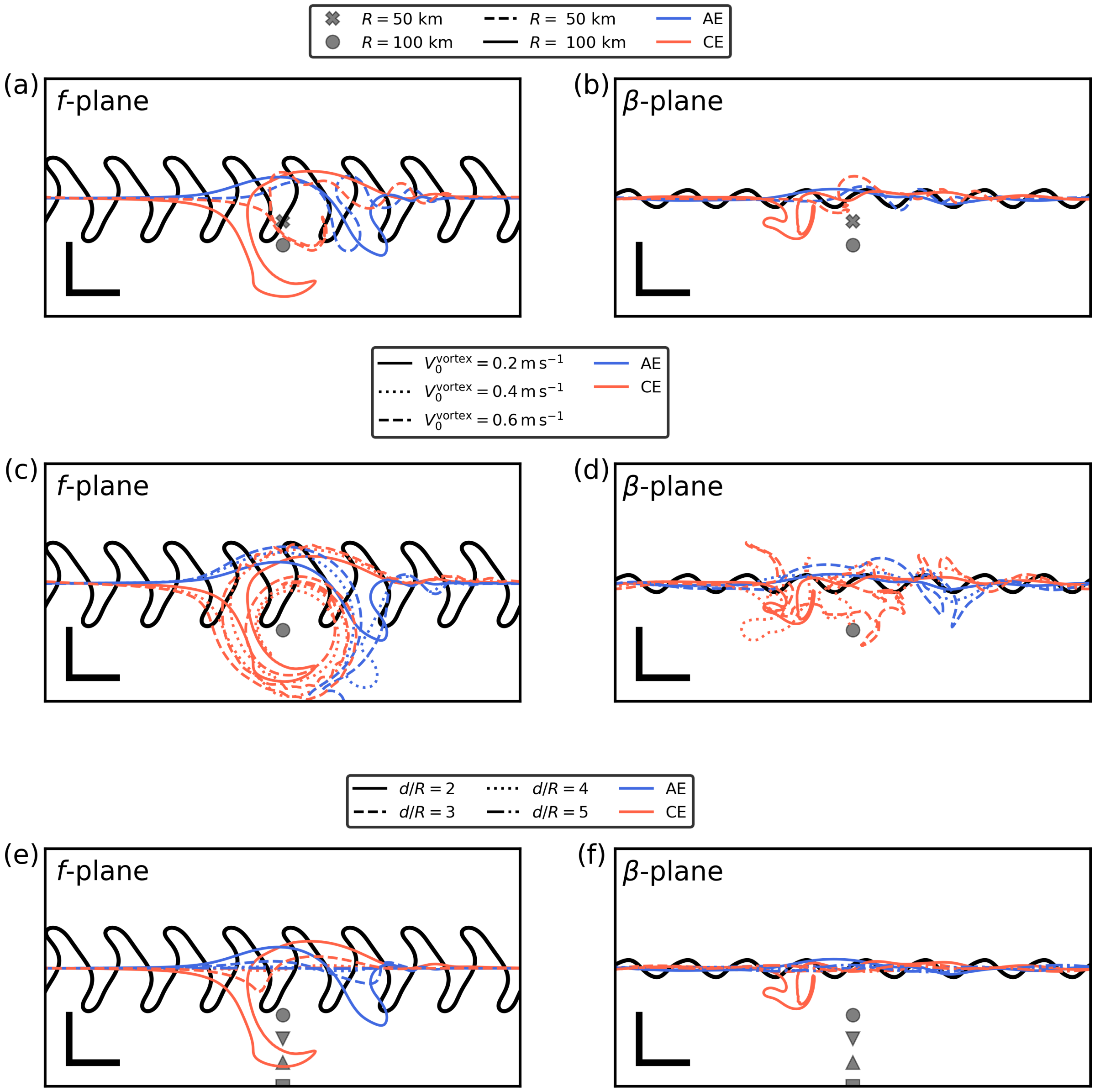

Figure 5: Position of the upwelling front (initially $L = 50$ km, $H = 200$ m, and $V_0^{\mathrm{up}} = 0.2\,\mathrm{m\,s^{-1}}$) at $t = 100$ days, in simulations with an isolated vortex of parameters (a,b) d/R=2, $V_0^{\mathrm{vortex}} = 0.2\,\mathrm{m\,s^{-1}}$, and different values of vortex radius R; (c,d) $d/R = 2$, $R = 100$ km, and different values of azimuthal velocity V_0^{vortex}; (e,f) $V_0^{\mathrm{vortex}} = 0.2\,\mathrm{m\,s^{-1}}$, $R = 100$ km, and different values of upwelling-vortex distance $dR/$. The left (resp. right) column shows simulations without (resp. with) β-effect. Note that for each column, solid lines of a given color show the same simulation. In all panels, black line shows the upwelling front initialized along with a sinusoidal perturbation (λ_{pert}=250 km), red (resp. blue) lines show the upwelling front initialized along with a cyclonic (resp. anticyclonic) vortex, markers show the initial position of the vortex, and sizebars in the bottom left show a distance of 200×200 km.

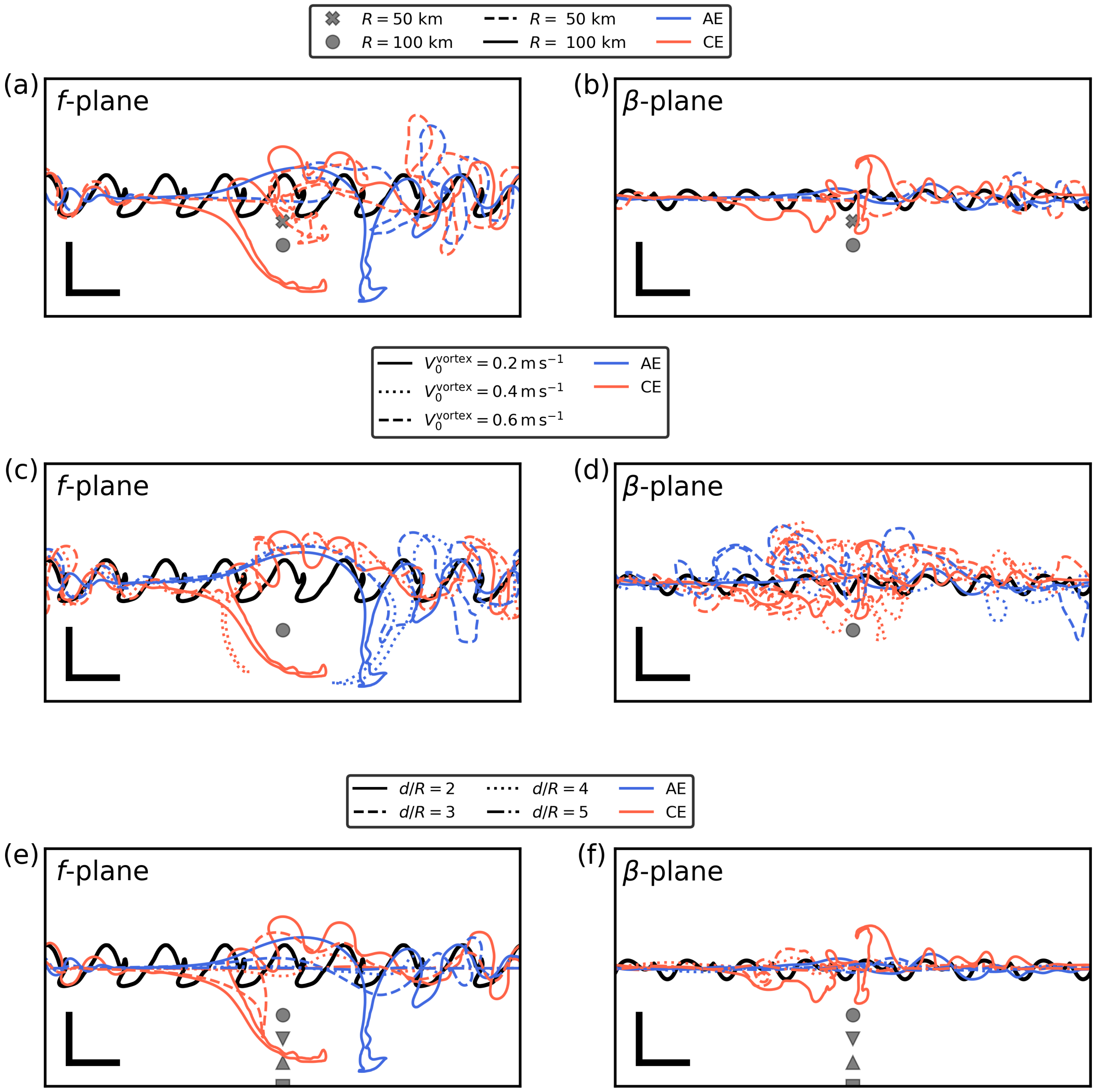

Figure 6: Same as Fig. 5 at $t = 200$ days

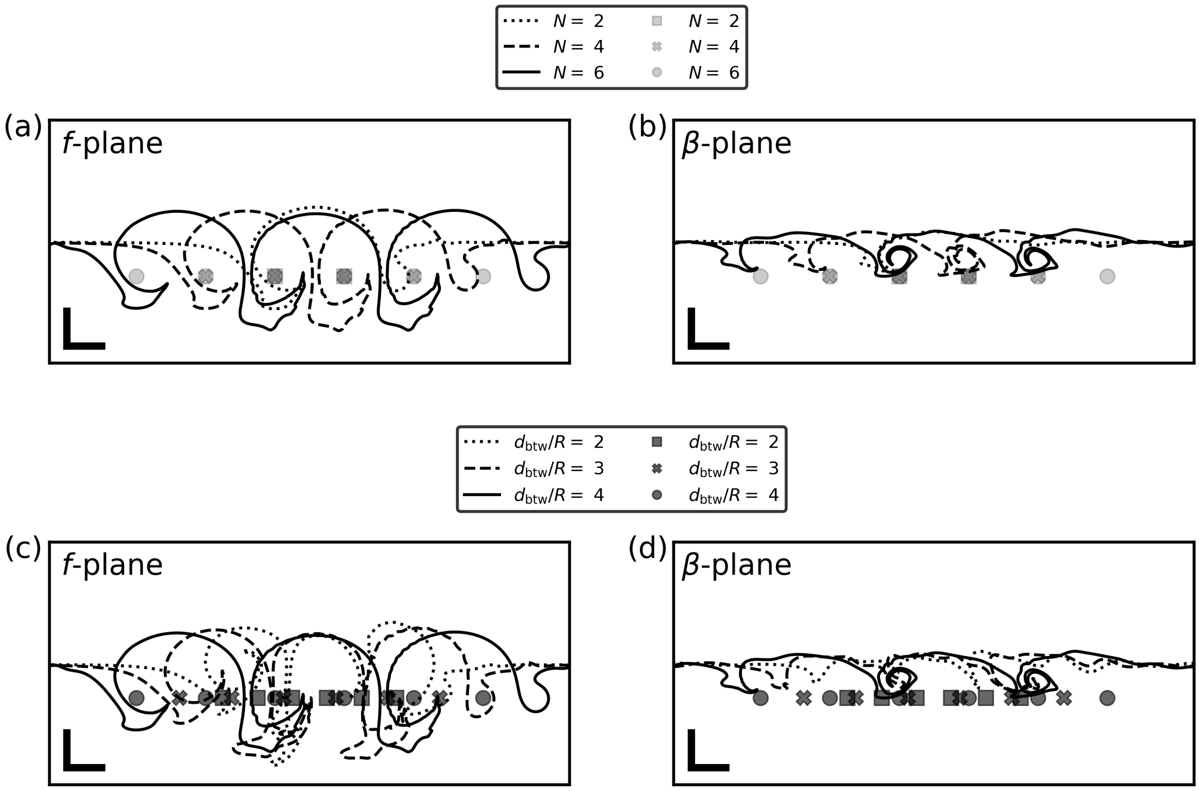

Figure 7: Position of the upwelling front (initially $L = 50$ km, $H = 200$ m, and $V_0^{\mathrm{up}} = 0.2\,\mathrm{m\,s^{-1}}$) at $t =$ 100 days, in simulations with a vortex alley of parameters (a,b) d/R=2, $V_0^{\mathrm{vortex}} = 0.2\,\mathrm{m\,s^{-1}}$, $R = 100$ km, $d_{\mathrm{btw}}/R = 4$, and different number N of vortices; (c,d) d/R=2, $V_0^{\mathrm{vortex}} = 0.2\,\mathrm{m\,s^{-1}}$, $R = 100$ km, $N = 6$, and different values of distance between vortices d_{btw}/R. The left (resp. right) column shows simulations without (resp. with) β-effect. Note that for each column, solid lines show the same simulation. Markers show the initial position of vortices, and sizebars in the bottom left show a distance of 200×200 km.

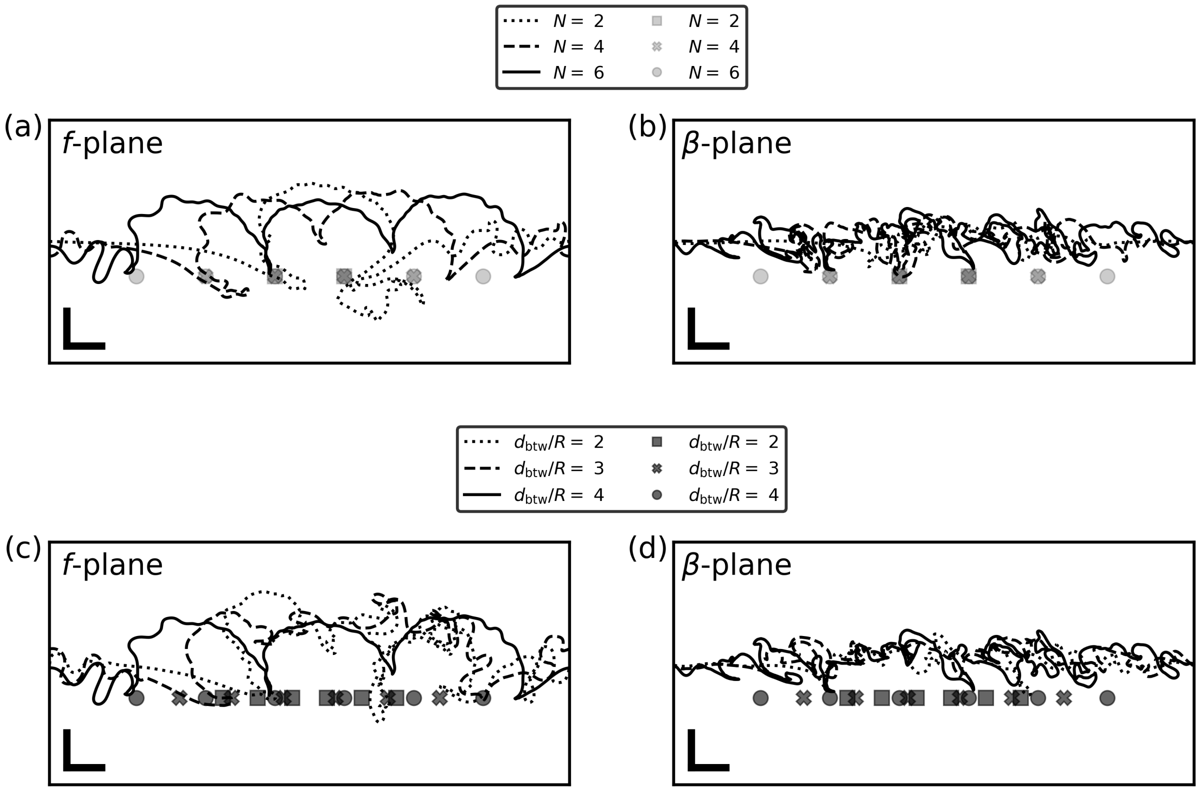

Figure 8: Same as Fig. 8 at $t = 200$ days

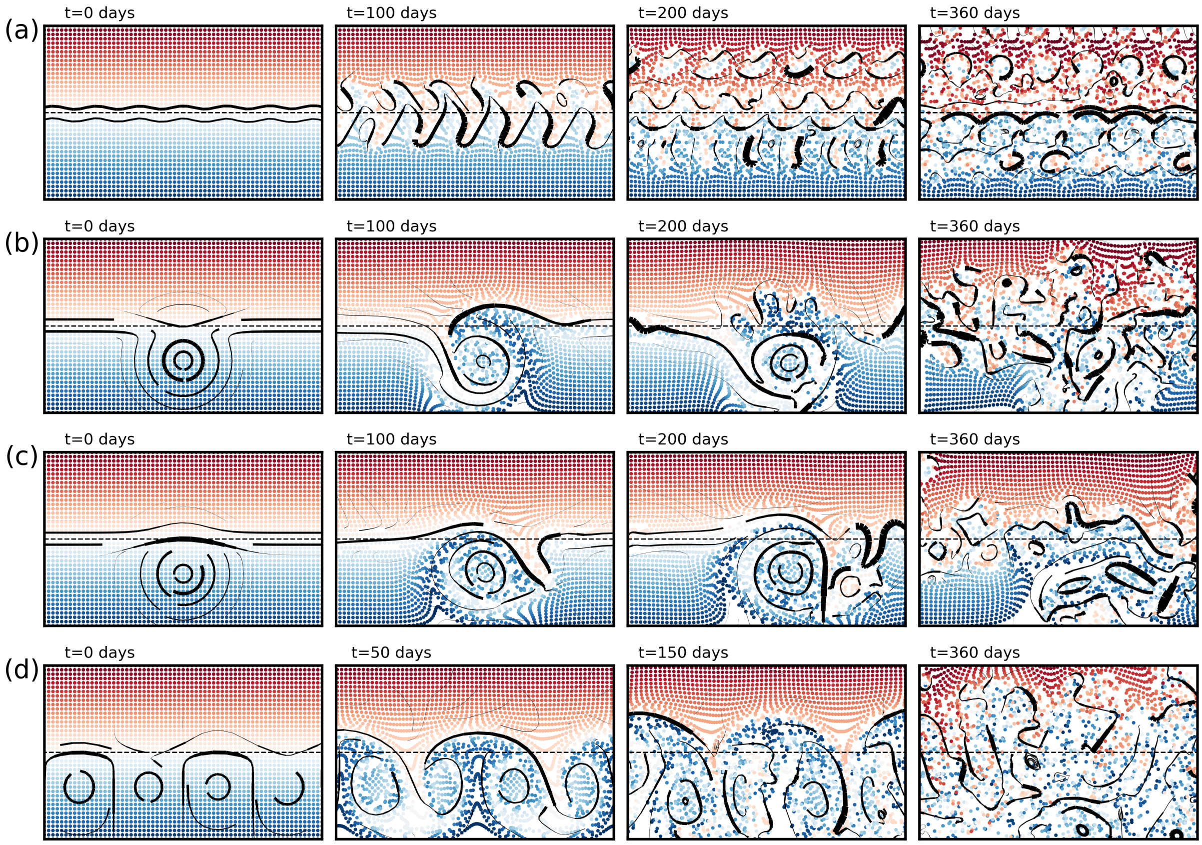

Figure 9: Snapshots of particle advection simulations with an upwelling front of parameters $L = 50$ km, $H = 200$ m, and $V_0^{\mathrm{up}} = 0.2\,\mathrm{m\,s^{-1}}$, and (a) a sinusoidal perturbation ($\lambda_{\mathrm{pert}} = 250$ km), (b, resp. c) an isolated cyclonic (resp. anticyclonic) vortex ($R = 100$ km, $H_{\mathrm{vortex}} = 1000$ m, $V_0^{\mathrm{vortex}} = 0.2\,\mathrm{m\,s^{-1}}$, and $d/R = 2$), and (d) a vortex alley ($R = 100$ km, $H_{\mathrm{vortex}} = 1000$ m, $V_0^{\mathrm{vortex}} = 0.2\,\mathrm{m\,s^{-1}}$, $d/R = 2$, $N = 6$, and $d_{\mathrm{btw}}/R = 4$). The particle color indicates the initial y-position of particles. Black solid lines show streamlines of the surface velocity field from the CROCO simulations used for the particle advection. Black dashed lines show the initial y-position of the upwelling front, that defines the frontier between off-shore (South) and on-shore (North) regions. Each panel is centered at the center of the domain and is 1600×1000 km wide.

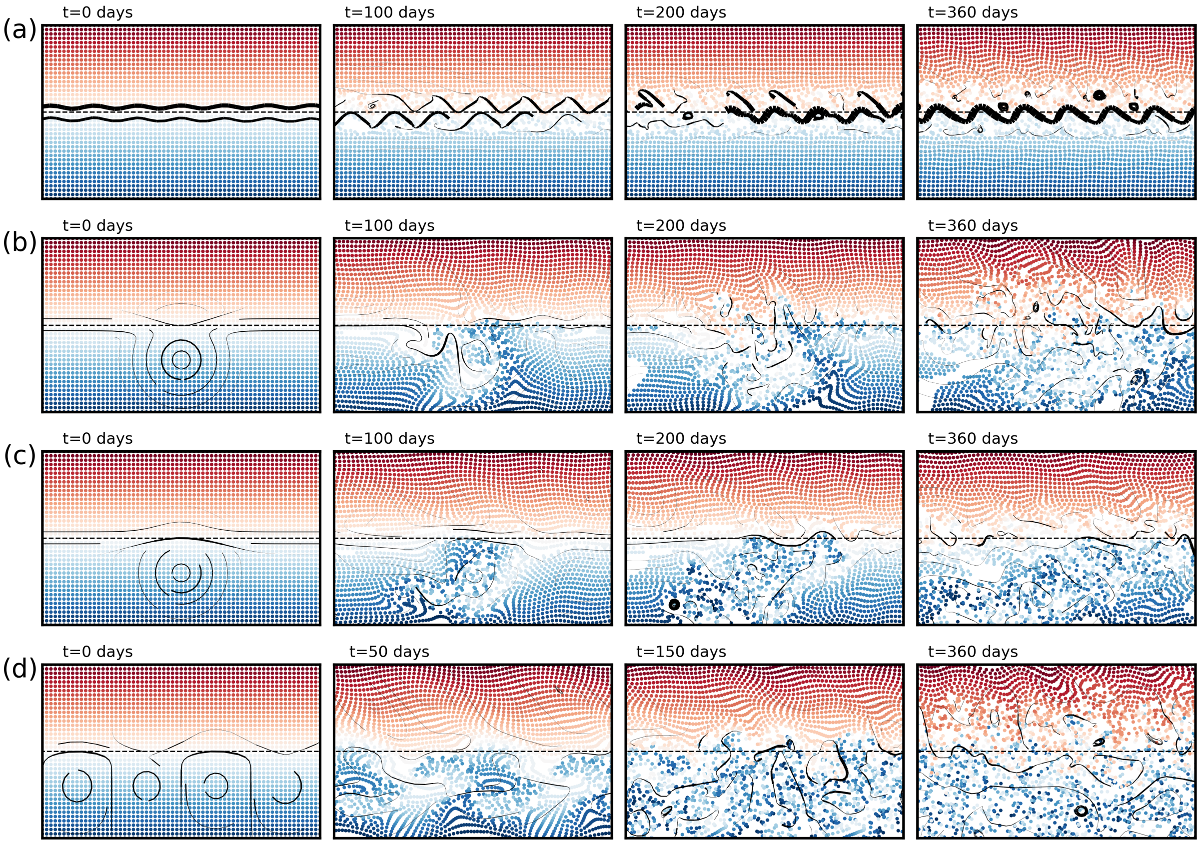

Figure 10: Same as Fig. 9 but with β-effect added in simulations.

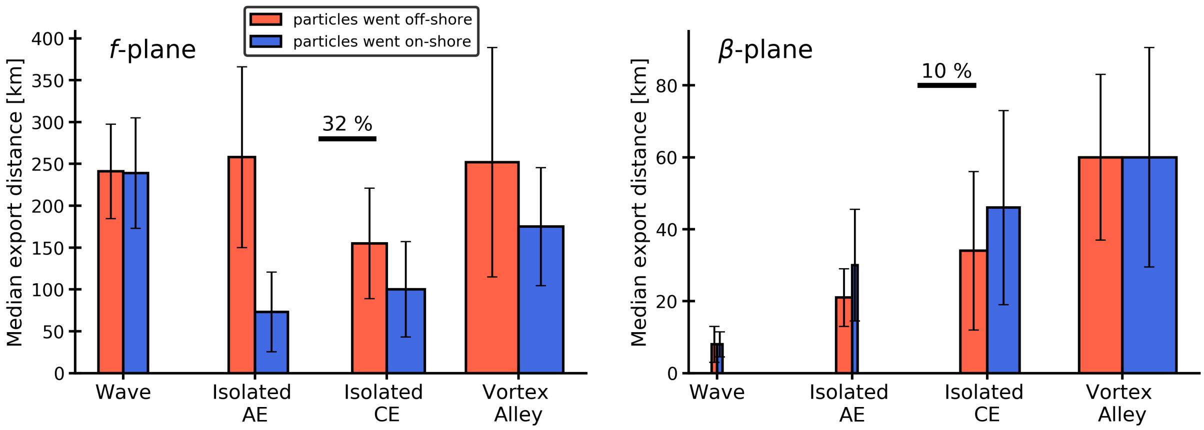

Figure 11: Median export distance of particles after one year of advection in different simulations on the f-plane (left) or the β-plane (right). Errorbars show the standard deviation of export distance, and width of boxes indicate the percentage of exported particles (see the size bar in each panel). Note that scales are different in each panel. All simulation have initially an upwelling front with $L = 50$ km, $H = 200$ m, and $V_0^{\mathrm{up}} = 0.2\,\mathrm{m\,s^{-1}}$; "wave" corresponds to simulations with a sinusoidal perturbation ($\lambda_{\mathrm{pert}} = 250$ km), "isolated CE (resp. AE)" corresponds to simulations with an isolated cyclonic (resp. anticyclonic) vortex ($R = 100$ km, $H_{\mathrm{vortex}} = 1000$ m, $V_0^{\mathrm{vortex}} = 0.2\,\mathrm{m\,s^{-1}}$, and $d/R = 2$), and "vortex alley" corresponds to simulations with a vortex alley ($R = 100$ km, $H_{\mathrm{vortex}} = 1000$ m, $V_0^{\mathrm{vortex}} = 0.2\,\mathrm{m\,s^{-1}}$, $d/R = 2$, $N = 6$, and $d_{\mathrm{btw}}/R = 4$). Note that simulations discussed in this figure are the same as simulations shown in Fig. 9 and in Fig. 10.

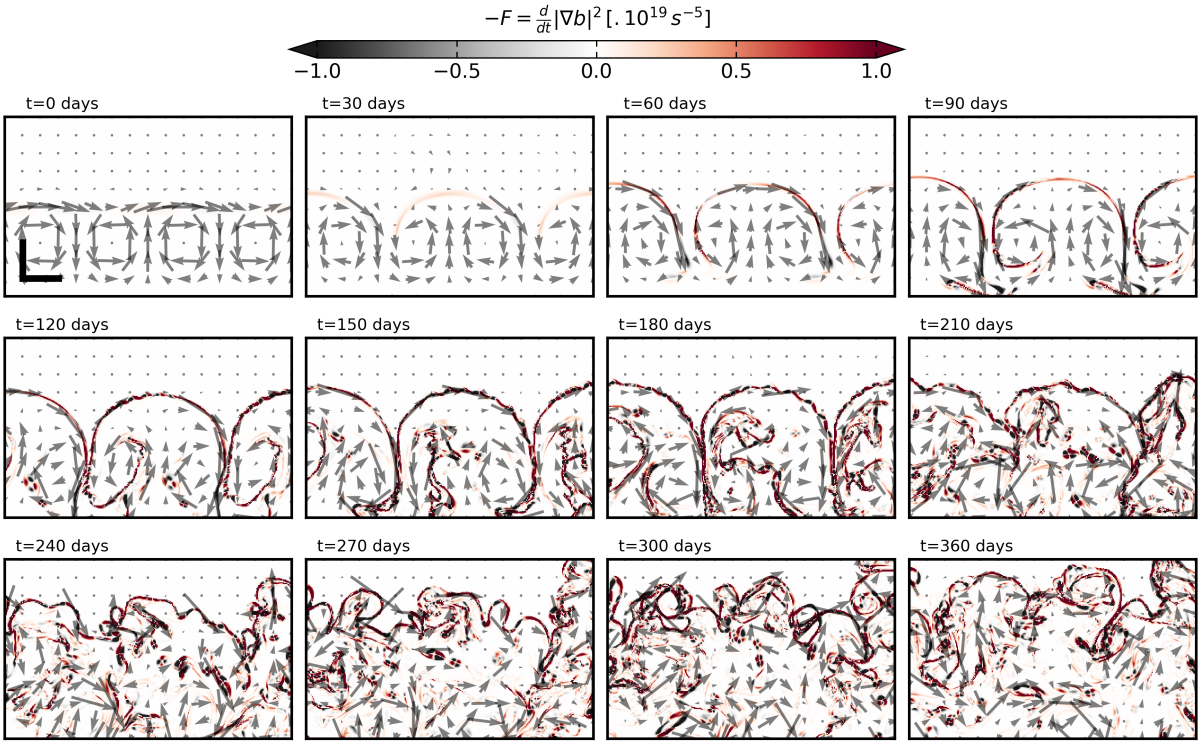

Figure 12: Time evolution of $-F$ in the simulation with an upwelling front of parameters $L = 50$ km, $H = 200$ m, and $V_0^{\text{up}} = 0.2\,\text{m}\,\text{s}^{-1}$, and a vortex alley ($R = 100$ km, $H_{\text{vortex}} = 1000$ m, $V_0^{\text{vortex}} = 0.2\,\text{m}\,\text{s}^{-1}$, $d/R = 2$, $N = 6$, and $d_{\text{btw}}/R = 4$), *i.e.* the "vortex alley" case in Fig. 11. Grey arrows show the surface velocity field. Sizebars in the bottom left show a distance of 200×200 km. Each panel is centered at the center of the domain and is 1600×1000 km wide.